Tomographic Reconstruction of Rolling Contact Fatigues in Rails using 3D Eddy Current Pulsed Thermography

Xiaotian Chen, GuiYun Tian, Song Ding, Junaid Ahmed and Wai Lok Woo

***Abstract*— The detection and quantification of the rolling contact fatigue (RCF) in rail tracks are essential for rail safety and condition-based maintenance. The tomographic reconstruction of the rolling contact fatigue is challenging work. The x-ray is unable to do in-situ inspection effectively. This paper proposes a new approach for RCF construction using 3D eddy current pulsed thermography. A differential time-square-root (sqrt) of temperature drop (DTSTD) is proposed as a mean to construct the sectional images and to reconstruct the thermal tomography image. The proposed method is validated through artificial angular crack slots as well as natural RCF crack. The thermal tomographic reconstruction is compared with the x-ray computed tomography on a rail track head cut-off with RCF cracks.**

***Index Terms*—thermal tomography, QNDE, 3D ECPT, DTSTD**

I. INTRODUCTION

Rail has always been considered as one of the safest mediums for traveling but it is seldom checked and monitored on the quality assurance until fatal accident happens [1]. During the investigation, it was found and concluded that rolling contact fatigue (RCF) is one of the main causes of accident. Therefore it becomes ever more important to monitor rails for such types of defects to avoid any further fatalities.

Up to now, many Non-Destructive Testing (NDT) techniques have been used for rail inspection. Clark [2] states that ultrasonic-based NDT has been performed for the surface and sub-surface defect inspection on the rail. However, this approach suffers from shadowing as the defect depth increases. Li et al. [3] proposed magnetic flux leakage (MFL) for high-speed defect detection in railways. A theoretical study with numerical simulation of different defects in motion mode was studied. Thomas et al. [4] proposed pulsed eddy current (PEC) for defect detection on rails. However, the PEC probes suffered degradation due to the lift-off effect. Nicholson and Davis [5] investigated the alternating current field measurement (ACFM) for rail inspection. It provided good results for surface defects, but had poor performance for sub-surface and multiple defects. Hirao and Ogi [6] used the electromagnetic acoustic transducer (EMAT) for rail defect quantification. However, this approach also suffered from deep defect depth.

In active thermography, eddy current pulsed thermography (ECPT) has actively been used for rail inspection and has been reported to detect weaker defects with higher sensitivity as compared with ultrasonic and laser-based NDT approaches [7]. RCF defects are difficult to detect and quantify due to their complex geometrical shape and tiny size. Mukriz et al. [8] quantified RCF as the angular defects and used PEC-based approach to quantify the defect angle information. However, other factors such as depth were not considered. Abidin et al. [9] used ECPT along with the amplitude and gradient information to quantify the angle as well as depth information. Peng et al. [10] used a similar approach with the addition of a Helmholtz coil for a non-uniform heating problem. All these approaches utilized two-dimensional technology to visualize and inspect the defects. However, due to the complex nature and geometry of the RCF involving depth and angle orientation, it became very difficult to interpret the results. To tackle this problem, normally repeatable experiments were carried out using the probability of detection approaches [11]. However, they tended to be very time-consuming and difficult to be implemented for online NDT.

The eddy current pulsed thermography (ECPT) is well used for defects detection, especially surface crack or corrosion detection and evaluation in conductive material. The infrared image sequence indicates the thermal distribution and heat diffusion process [12]. In the ECPT experiment, the transient thermal response of ECPT contains rich information on the crack characteristics. Previous work has well studied the features for cracks defection and characterization from the pixel level features [13], local area features [14] to the pattern level features such as Principal Component Analysis (PCA) and Independent Component Analysis (ICA) [15]. These works provide qualitative evaluation of the characteristics of the defect. Based on these works, a recent study [16] discussed feature-based quantitative relationship of defect size (depth and length) and their thermal responses.

Alternative to feature-based QNDE for ECPT images, in [17] electrical and thermal conductivities are estimated by the early

This work is partially supported by National Natural Science Foundation of China (Grant No.61527803, and Grant No.51505308) and International Science and Technology Innovation Cooperation Project of Sichuan Province, China (Grant No. 2021YFH0036).

X. Chen is with School of Mechanical Engineering, Sichuan University, Chengdu, China.

G. Tian is with School of Engineering, Newcastle University, United Kingdom.

Song Ding is with School of Electrical Engineering and Control Science, Nanjing University of technology, Nanjing China.

J. Ahmed is with Electrical Engineering Department, Sukkut IBA University, Pakistan.

W.L. Woo is with Department of Computer and Information Sciences, Northumbria University, United Kingdom.

experimental transient response of the first layer having a visible fiber's orientation. An iterative inverse procedure is used to minimize the discrepancy between measured and simulated data to reconstruct orientations of each layer using the estimated conductivity. However, no work up until now has discussed the geometry of undersurface cracks. This paper proposes a novel approach to reconstruct 3D images and evaluate the morphological localization of subsurface cracks based on 2D thermal slices. Differential time square root (sqrt) of temperature drop (DTSTD) is extracted to characterize the shape of the subsurface crack along with the crack sizing, depths, and validated.

With the recent advancement of NDT in 3D reconstruction based tomographic approaches for internal and sub-surface defects, the qualitative and quantitative analysis of RCF types and shapes becomes a crucial and urgent task. In contrast to conventional approaches, the x-ray based CT shows better resolution results and defect depth estimations. The different case studies of the use of x-ray CT for NDT have been proposed in [18]. The x-ray based CT produces good results for depth estimation in NDT problems. However, the equipment is expensive and bulky along with the risk of radiation effects if continuously used. Also, it is difficult for x-ray to penetrate the entire rail which makes it hard to use x-ray CT for online inspection of RCF cracks. The high-energy industrial CT (above 4Mev) could penetrate the entire rail track head. However, the higher the energy of the x-ray, the lower the resolution (for 4Mev, the resolution is 1mm), which makes it impossible to identify the RCF cracks in the rails. For the ultrasonic approach, Daigle et al. [19] used an ultrasound-based 3D tomography approach for NDE of concrete structures.

Computed tomography is a well-established approach used to reconstruct cross-sectional slices through an object from the transmitted projection images taken as a function of angle around a single axis of rotation. In [20], the authors carried out different experiments using single view cone beam x-ray computed tomography to generate different datasets that can be used for supervised learning. A complete data reconstruction model was also presented. In [21], the single view based computed tomography was proposed. This approach had high-speed inspection but limited data acquisition time. Also, the generated tomographic sequences suffer from poor image quality and noise. Therefore to improve the reconstruction quality, different types of reconstruction algorithms have been proposed such as Artificial Intelligence (AI) based algorithms [22], total variation decomposition algorithm [21], truncated singular value decomposition algorithm [23], and wavelet-based algorithm [20]. The single-side view tomography is a recent and newly developed technique with the help of computing models and AI [22]. These slices can be stacked to produce a 3D image of the object, which can then be visualized by one of several methods, including volume rendering or digital slicing through the sample along any arbitrary plane [20-21]. These tomography techniques also boosted the development the thermal tomographic reconstruction and motivated the tomographic reconstruction of the 3D ECPT system.

The paper is presented as follows: Section II describes the 3D ECPT system set up, visualization and fusion pipeline. In Section III, we illustrate the ECPT thermal sequences behaviors and thermal propagation. In this section, we also propose the 3D tomography scenario and include the evaluation of the proposed work. Finally, the work is summarized in Section IV along with future work.

II. THE 3D EDDY CURRENT PULSED THERMOGRAPHY AND VISUALIZATION PIPELINE

The hardware setup of the proposed 3D ECPT is shown in Fig. 1. The signal generator sends a pulse to the active induction heater and the infrared camera. The coil carries high-frequency alternating current to produce an alternating magnetic field in the testing object. In this work, the Helmholtz coil and line coil are used as excitation coil for different geometry shapes of the testing structures. The eddy currents are therefore induced in the testing sample and the heat is generated on the sample surface and propagated to a certain thermal diffusion depth. The thermal image is captured by the infrared camera and the RGB-Depth image is captured by the David 3D system [24]. The thermal image is registered to the 3D scanner using a feature-based method provided in [25].

Fig. 2 shows the visualization and processing pipeline of the proposed method. After the thermal-depth image registration, the set of records of thermal image sequences $(temperature, time)$ with physical location coordinates (x, y, z) are recorded. To show the temperature response in different time slots, the normal vectors from the acquired point cloud surface are calculated. The temperature responses in the different time slots are visualized in the normal direction towards the surface in different depths noted as normal depth (N_d). These normal depth vectors are organized in a time-based manner and the temperature responses in the same time slot are placed in the same layer. As a result, it is visualized as each thermal image in a later time slot overlays the thermal image of the previous time slot. The final merged point cloud is down-sampled and the region of interest is adjusted to give a better perception of the defective area and non-defective area. The visualization software platform is designed using the point cloud library (PCL) via C++.

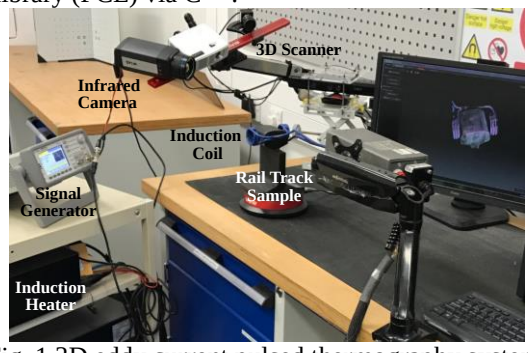

Fig. 1 3D eddy current pulsed thermography system

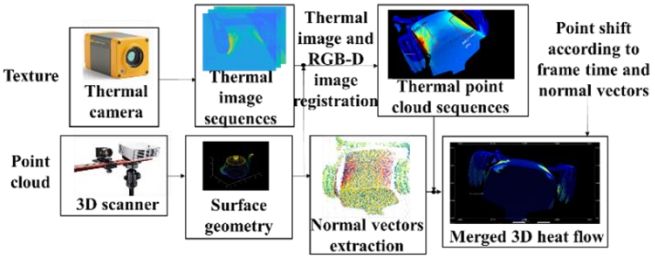

Fig. 2 Proposed pipeline of 3D fusion and visualization

III. THERMAL BEHAVIOR ANALYSIS AND RECONSTRUCTION

The research on computed tomography is mostly considered using the x-ray. Thermal tomography is difficult to conduct because the thermal energy not only penetrates vertically but also horizontally. Also, the thermal image is blurred which gives the harsh challenge of identifying tiny cracks like RCF cracks. Thus we are considering selecting the exciting heating source that maximizes the vertical heat penetration and minimizing the horizontal heating penetration while maintaining the resolution of the thermal patterns. In this paper, the pulsed eddy current is used. During the pulsed magnetic excitation, the eddy current is generated and it gathers at the edge position of the defects. The advantage over other NDT techniques is that the thermal propagation enlarges the defective area which allows the tiny defects like RCF detectable while it is very hard to recognize using X-ray or ultrasonic. However, the uneven volume heating of the eddy current results in the horizontal propagation which renders the analysis more complex compared to surface heating of flash thermography. To limit the horizontal propagation while balancing the resolution of enough induced current in the crack area, a maximum thermal rise of 3~4 centigrade is found to be the optimal setting during the experimental study. The steps of reconstruction and validation process is illustrated in Fig. 3.

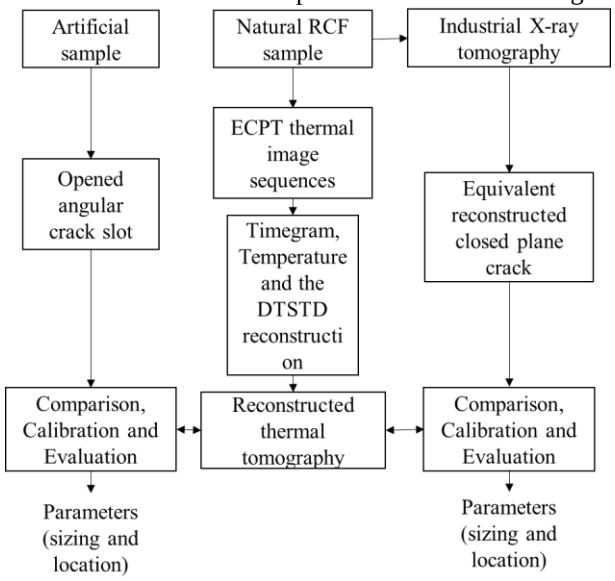

Fig. 3 Procedures for the reconstruction and validation of the DTSTD based thermal tomography for artificial and natural defects

Fig. 3 outlines the procedures and the validation of the proposed method. Section 3(a) illustrates the proposed method. Section 3(b) shows the reconstruction of an opened angular crack slot. The angular slot with different sizes is shown and compared with the up-to-data dynamic thermal reconstruction (DTT) technique. Section 3(c) gives the thermal tomographic reconstruction of the RCF in a rail track head cut-off. The thermal tomographic reconstruction is compared with the x-ray industrial computed tomography image.

a) Methodology of the DTSTD thermal tomography reconstruction

In the heating stage. The induced eddy current decays exponentially and penetrates to a certain depth. The penetration depth is given as

$$\delta = \sqrt{\frac{1}{\pi\sigma\mu\mu_0 v}} \tag{1}$$

where v is the frequency of the eddy current, μ and μ_0 are the relative permeability and the permeability of vacuum respectively, σ is the material conductivity. In the heating stage, the current penetration depth is very small. In our experiment, the steel material with an excitation frequency of 200 kHz has a skin depth of only 0.03mm. Thus the heat energy is only distributed at the surface region. Fig. 4(a) is the image taken at the end of the heating stage. The surface cracks are the major factors that cause the thermal discontinuities in this stage.

After the heating stage, only the heat conduction in steel is considered in the cooling stage due to the conductivity of air ($0.023\ W/m\cdot K$) is far less than that of steel ($\sim 47 W/m\cdot K$). The heat conduction speed in the steel material is quicker [35]. The speed of heat penetration is given as

$$d_{heat} = 2\sqrt{kt} \tag{2}$$

where k is the thermal diffusivity and t is the elapsed time. For the steel material, the heat penetrates up to 5~7mm in one second. Thus, in the cooling stage, the first few frames show the surface crack information while the later frames show more of the sub-surface information as the heat penetrates the testing object. Fig. 4(a) shows the 3D heat distribution at the beginning of the cooling stage.

Eq. (2) builds the relationship of time and heat penetration depth and shows that the heat penetration depth is proportional to the root square of time and the material thermal diffusivity. For a specimen like a rail track which is constructed of steel, the thermal diffusivity can be treated as constant. Similar to the x-ray computed tomography, Eq. (2) shows that the penetration depth is proportional to the square root (sqrt) of elapsed cooling time. This paper uses the sqrt time of temperature drop for depth estimation.

Figs. 4(c) and (d) show the visualization of sqrt time drop to the a℃, a=60% temperature drop (mean temperature of the heat flow). The new point coordinate is given by

$$P_{T=a℃} = \begin{bmatrix} x_t \\ y_t \\ z_t \end{bmatrix} = \begin{bmatrix} x_0 \\ y_0 \\ z_0 \end{bmatrix} + 2\sqrt{kt_{(x_0,y_0,z_0,T=a℃)}} \begin{bmatrix} x_n \\ y_n \\ z_n \end{bmatrix} \tag{3}$$

where (x_0, y_0, z_0) is the point coordinate on the surface, (x_n, y_n, z_n) is the normal vector of the surface at (x_0, y_0, z_0); $t_{(x_0,y_0,z_0,T=a℃)}$ is the elapsed time to reach to a temperature layer at the position (x_0, y_0, z_0).

In Figs. 4(c) and (d), the height of the point cloud leaves the surface is proportional to the square root time of temperature

drop, which is also the position where the heat penetrates. Fig. 4(c) shows the top view of the 3D sqrt time of temperature drop image while Fig. 4(d) gives the bottom view. Considering these time images together with Fig. 4(a), the 3D thermal distribution in Fig. 4(a) shows the thermal patterns of the surface defect distribution since the heat has not been penetrated into depth at the beginning of the cooling stage. The major cause of the thermal discontinuity in Fig. 4(a) is the high current density in the crack area during the heating stage. Fig. 4(b) shows the temperature layers in different colors and the time arrival to this layer is the height to the surface. Fig. 4(c) and (d) are the 3D visualization of the time images in later frame with a cut-off temperature of 70% maximum temperature drop. The cut-off temperature stand for all pixels are in the same temperature level which is 70% of maximum temperature drop. These images use the information in later image sequences where the heat has penetrated into the material at a certain depth. The discontinuity (different time arrival to this temperature level) is mostly caused by the subsurface cracks. The heat penetration depth is calculated using Eq. (2). The following section describes the proposed method for computing the response signal when the heat reaches the depth level.

Fig. 4(a) shows the 3D heat flow at the maximum temperature frame (time slot right after the heating stage). The experiment setup was shown in previous work [25]. The Easyheat 224 from Cheltenham Induction Heating is implemented for the coil excitation. The Helmholtz coil with water cooling is selected. The water is pumped through the coil copper tube during the experiment. The excitation frequency is 200kHz in 300A. The heat flow is recorded by the FLIR SC7500 which has an In Sb detector of infrared range between 1.5~5 μm. The camera has a pixel resolution of 320×256 and a maximum speed of 383Hz. The thermal camera utilizes a maximum speed rate of 383Hz. The heating time is 200ms and the cooling time is 800ms. The testing sample is a rail track sample with rolling contact fatigues on one side of the rail track shoulder.

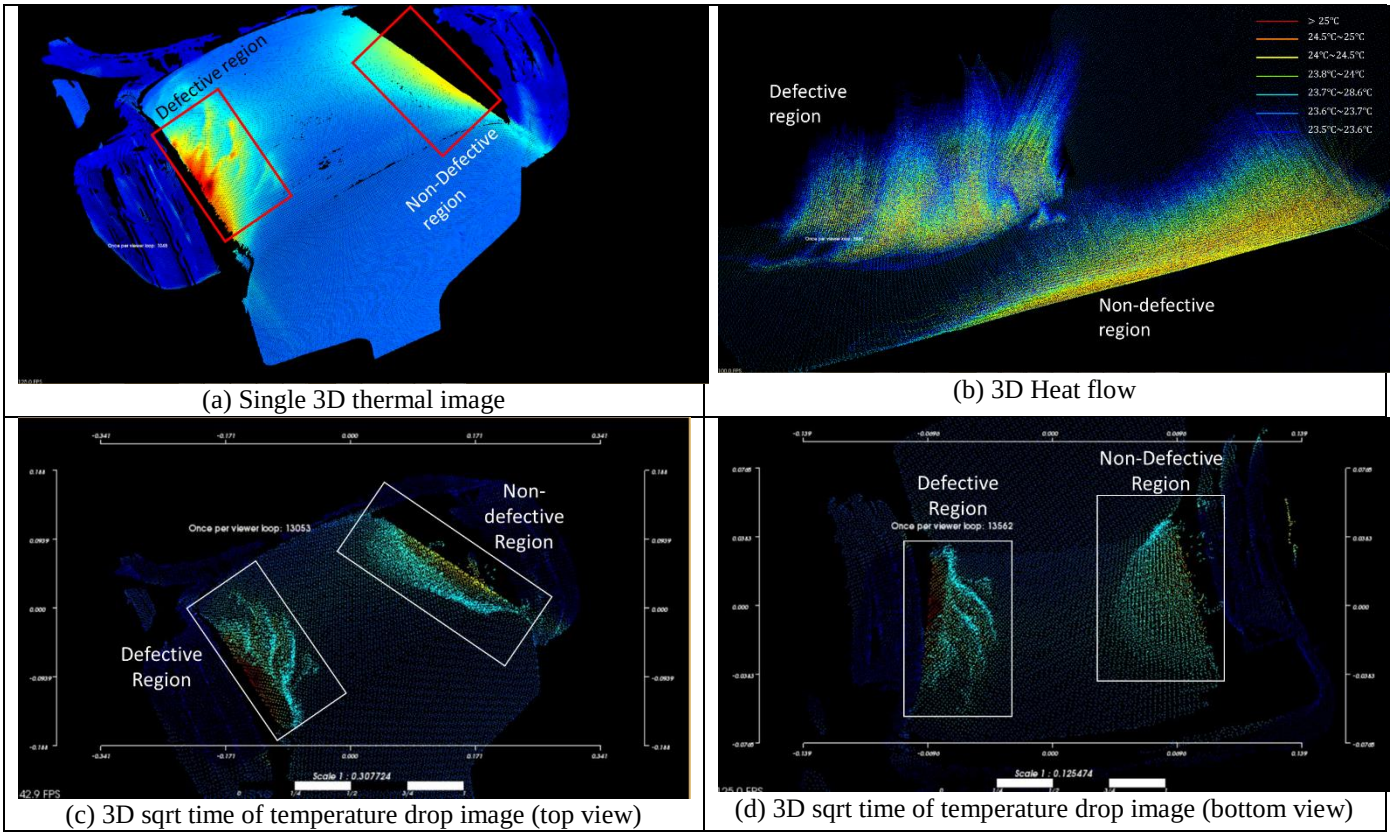

Fig. 4 Visualization of the 3D heat flow. (a) Single 3D thermal image; (b) 3D Heat flow; (c) 3D sqrt time of temperature drop image (top view); (d) 3D sqrt time of temperature drop image (bottom view)

To enhance the contrast between the defective region and the non-defective region, the point cloud is down-sampled. Using the fusion method provided in Section II, the fused 3D heat flow is generated and shown in Fig. 4(b). This figure merges the 3D heat flow into one single image frame. The fused 3D heat flow in Fig. 4(b) presents the following information: (1) The surface temperature distribution at the maximum temperature frame is given at the surface of the rail track; (2) the thermal images in later time slots are placed as plane layers overlay the previous time slots; (3) the images taken at different time slots is visualized in one single 3D image. In this figure, different temperature layers from 10% maximum temperature drop to 80% are marked with different colour while the height of the layer indicates the time arrival to this temperature (top 10%

temperature range and bottom 20% temperature range are ignored because of too much noise information). It could be seen that the defect-free area has a very uniform time arrival shape while the defect area is clustered into several scattered regions.

In addition, the time cost from each layer to the next layer is visualized as the width of the temperature zoom. A higher time cost of the temperature layer indicates a defect exists in this layer. Using such a system as a base, a thermal tomography system is proposed using the differential square root of temperature drop as pictured in Fig. 5.

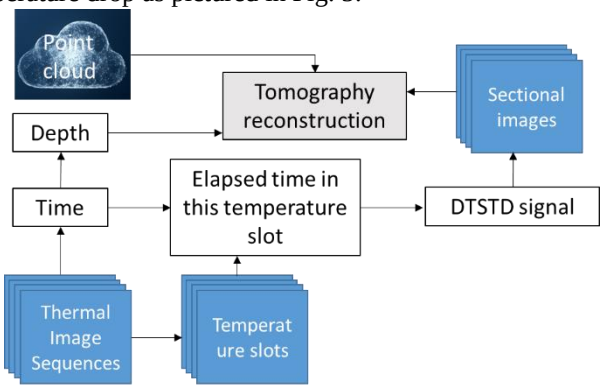

Fig. 5 Proposed DTSTD algorithm

The analysis starts from form of heat conduction as:

$$\frac{\partial T}{\partial t} = \alpha_x(x)\frac{\partial^2 T}{\partial x^2} + \alpha_y(y)\frac{\partial^2 T}{\partial y^2} + \alpha_z(z)\frac{\partial^2 T}{\partial z^2} \quad (4)$$

The thermal distribution in any position of a body can be calculated if given the structure of the body, its boundary condition and its initial states. The boundary condition in thermal conduction is a differential equation that describes the thermal conduction between the body with other materials. The initial state describes the temperature distribution at the time $\mathrm{t} = 0$. The $\alpha_x, \alpha_y, \alpha_z$ are the thermal diffusivity at the $\mathrm{x}, \mathrm{y}, \mathrm{z}$ direction and the thermal diffusivity describes the ability to pass the temperature to its surroundings. The thermal diffusivity $\alpha(m^2/s)$ is already discussed in the paper where

$$\alpha = \frac{k}{\rho c} \quad (5)$$

$\mathrm{k}(\mathrm{W/m \cdot k})$ is the thermal conductivity that describes the ability of heat energy transportation. The thermal conductivity k is also used to evaluate the depth of heat propagation as $d_{heat} = 2\sqrt{kt}$. The $\rho(\mathrm{kg}/m^3)$ is the material density and $\mathrm{c}(\frac{\mathrm{J}}{\mathrm{kg}} \cdot \mathrm{k})$ is the material's heat capacity which describes the amount of heat absorbed with a unit of temperature change. Currently only the numerical solution of Eq. (4) is provided using the finite element method (FEM). The analytical solution only exists for a few ideal cases. One of the analytical solutions of Eq. (4) is based on one of the ideal cases where an ideal heat pulse is evenly spread on the structure surface. The structure of the body is a semi-infinite solid plate. The analytical solution of the ideal situation is given by:

$$T(z,t) = \frac{Q_0}{\sqrt{t\pi}\zeta} e^{\left(-\frac{z^2}{4\alpha_z t}\right)} + T_a \quad (6)$$

where ζ is the thermal effusivity which is the measurement of its ability to change the thermal energy with its surrounding. Q_0 is the total energy of the pulsed excitation. T_a is the ambient temperature. As stated previously, the ambient temperature is eliminated by the background subtraction. The active thermal image sequences are subtracted with 'inactive states' which is the state without heating. Since the thermal camera only captures the thermal responses in the surface layer, The recorded thermal depth $\mathrm{z} = 0$. Substituting these parameters into Eq. 6 gives:

$$\Delta\mathrm{T(t)} = \frac{Q_0}{\sqrt{t\pi}\zeta} \quad (7)$$

Take the log in both left and right side gives

$$\log\big(\Delta\mathrm{T(t)}\big) = \log\left(\frac{Q_0}{\sqrt{t\pi}\zeta}\right)$$

$$\log\big(\Delta\mathrm{T(t)}\big) = \log(Q_0) + \frac{1}{2}\log(\mathrm{t}) - \log\big(\sqrt{\pi}.\zeta\big)$$

$$\log(t) = 2\big(\log(Q_0) - \log\big(\sqrt{\pi}.\zeta\big) - \log\big(\Delta\mathrm{T(t)}\big)\big) \quad (8)$$

Given that Q_0 is constant. The temperature $\Delta\mathrm{T(t)}$ is the same in each temperature layers. Eq. (8) gives the relationship that the thermal effusivity is directly link to the thermal penetration time where the thermal effusivity ζ is directly related to the crack characteristic.

As for the penetration depth, it is found the time relationship and the penetration depth. Theoretically, the more time it cost to reach the temperature level, the higher of thermal diffusivity is which reveals there exists one or several cracks under the surface. For different temperature layers, a higher time cost to the next temperature level indicates that there exists a discontinuity that blocks the heat transfer. The elapsed time in each temperature layer is used as the response signal for the reconstruction of the sectional images. Fig. 6. shows the differential sqrt time of temperature drop images, where

$$\mathrm{R(u,v)}_d = \sqrt{T_{a\%\mathrm{C}}} - \sqrt{T_{b\%\mathrm{C}}} \quad (9)$$

In Eq. (9), the R(u,v) is the response signal at a pixel location (u,v). The subscript d denotes the penetration depth where the heat penetrates to the cut-off temperature a % ℃ temperature drop . The term $T_{a\%\mathrm{C}}$ is the sqrt temperature drop reaching cut-off temperature a℃ and $T_{b\%\mathrm{C}}$ is the sqrt temperature drop reaching cut-off temperature b%℃. Figs. 6 a~g shows the differential sqrt time of temperature drop from the range of 10% temperature drop to 80%. These time images contain both depth and intensity information of the cracks. For fig.6 (g), firstly, the sqrt of time cost to reach 80% temperature drop is calculated to estimate the heat penetration depth. Secondly, a strong pixel in Fig. 6(g) indicates a high time cost from heat level 70% to 80%, which indicates a crack under the current penetration depth.

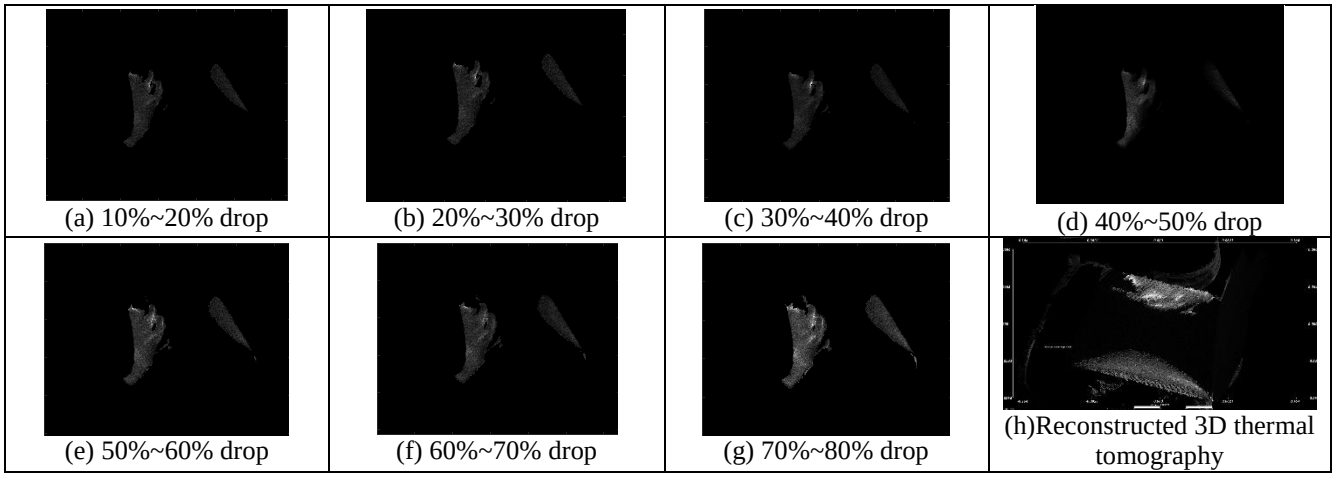

Fig. 6 Sectional images and the reconstructed 3D thermal tomographic image (top view)

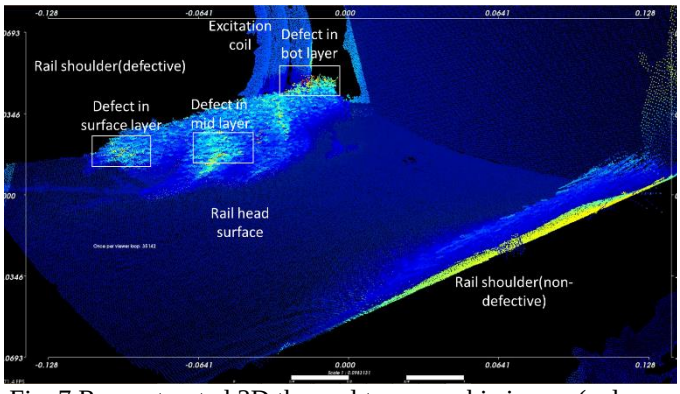

Fig. 7 Reconstructed 3D thermal tomographic image (color map in jet)

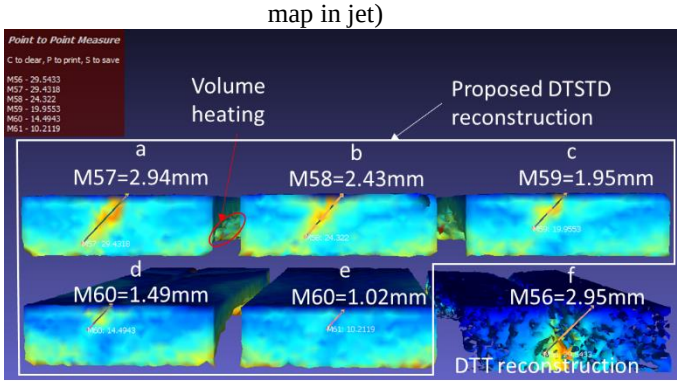

Fig. 8 Comparison of reconstructed artificial angular crack slot using DTSTD and DTT

Same principles as shown in Fig. 6(g), Figs. 6(a) to (f) are the differential square root time images at different temperature layers from 80% temperature drop to 10%. Fig. 6 (g) has the deepest thermal penetration depth since the time to reach the 80% temperature drop is the longest in all image sequences, where Fig. 6(a) has the least penetration depth for the same reason. From the time-image sequences, it can be seen that the deeper the penetration depth, the more detail and contrast the image is. This observation is opposite to the obtained ECPT thermal images sequences as these thermal image has the highest contrast in early cooling time and become blurred in the later cooling stage. The reason is due to the fact that at the beginning of the cooling stage, the thermal image has the maximum temperature divergence caused by the non-uniform heating and the higher current density in the defective area. However, the large temperature divergence also results in a quick temperature drop which eventually leads to a small-time interval between each temperature layer. The small-time interval will result in a low resolution of the differential square root time images in Figs. 6. Thus, the DTSTD sectional images have higher contrast in the later cooling stage and ECPT thermal image sequences has higher contrast at early cooling stage. Given the intensity images with different time slots shown in Figs. 6(a~g), the 3D positions with intensities (x, y, z, i) are calculated using Eq. (9), where i is the intensity of images Figs. (a~g) and t is the elapsed time to each temperature level from 10% temperature drop to 80% temperature drop. The reconstructed 3D tomography image is shown in Fig. 7.

B) Reconstruction of the angular crack slots and comparison with dynamic thermal tomography

The dynamic thermal tomography (DTT) technique is the method for flash thermal tomography in the reconstruction of the defect structure [28~29]. The DTT reconstruction is also presented for comparison study. In the evident form the thermal effusivity given by $e = \sqrt{\lambda \rho C_\rho}$ where λ is the thermal conductivity, ρ is the material density and C_ρ is the material thermal conductivity. The thermal effusivity is to measure the ability of the heat propagation with its surroundings. For a semi-infinite body, the solution of thermal effusivity is given by:

$$e = \frac{W}{T\sqrt{\pi\tau}} \tag{10}$$

where W is the absorbed power, T is the surface temperature, τ is the elapsed time. Obviously, the crack region has a much lower thermal effusivity compared with defect-free region. Thus the thermal effusivity is used for the reconstruction of the slice images. Since the absorbed energy is hard to measure in the experiment accurately, the normalized effusivity is used given as:

$$\frac{e}{W} = \frac{1}{T\sqrt{\pi\tau}} \tag{11}$$

In this paper, the artificial angular crack slot is used with angular cracks from 1mm to 3mm and angle of 45°. The reconstructed tomography image is shown in Figs 8. (a~e) correspond to cracks of 1mm to 3mm reconstructed by the proposed DTSTD method. The high intensity voxels (shown as

red color) indicate a high DTSTD value. Image f is the 3mm crack reconstructed with reciprocal of the normalized thermal effusivity $\frac{W}{e}$. The stronger the intensity, the lower the effusivity where indicates the defect region. From Figs 8. (a~e), they show a 98.3% measurement accuracy of defect depth and angle where *error = mean(measured depth – real depth) / mean(measured depth).* The arched structure of the reconstructed image is caused by the even heating and thermal images with low time response in these temperature regions. Both DTT and DTSTD methods are used for the estimated reconstruction of the defect 3D structures. Since the DTT method is strictly derived from the semi-infinite model and the heat is assumed evenly spread on the test object surface, the DTT method used here suffers from non-uniform heating of the ECPT system. The proposed DTSTD method shown in Figs. 8(a~e) performs better with increased robustness to non-uniform heating while preserves enough reconstruction resolution compared to the DTT method. Fig. 8(f) shows reconstructed defect 3D structures with dynamic thermography where the depth and position of the defect are also visible. Although DTT method is good for surface heating, it performs inferior for volume heating of ECPT systems compared to the DTSTD method. The boundary effect is particularly critical and caused by the un-uniform heating of the ECPT system. The area near the excitation coil has a much stronger signal intensity compared to the area far from the excitation. The obtained result from artificial cracks shows the proposed method shows better performance in ECPT thermal tomography for the volume heating.

C) Comparison of x-ray computed tomography and proposed thermal tomography

This section validates and reports the comparison of the result from x-ray CT and the proposed thermal tomography approach. As is illustrated previously, the x-ray is hard to penetrate the entire rail track head. In this experiment, the rail track head with RCF is cut with a depth of 9mm. Fig. 9 (a) is the tomography image of an RCF cut-off sample reconstructed from X-ray CT. Fig. 9(b) is the proposed thermal tomography image. From the two images, D5 has the longest length and depth. The defects of D2 to D6 are well-matched with each other. However, For Fig. 9(b), the D1 and D7 are not well reconstructed and show large noise around due to the boundary effect of heat conduction, which shows that the edge effect and thermal propagation at borders should be reconsidered.

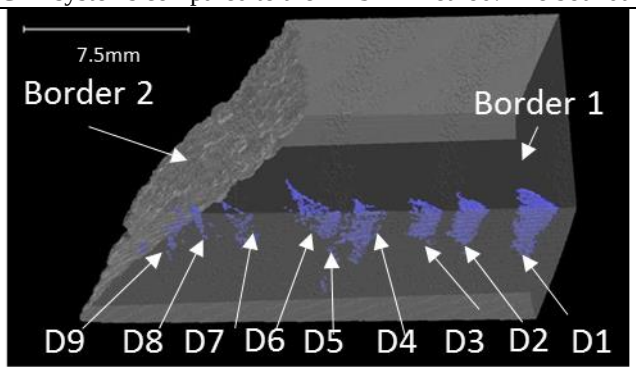

(a) X-ray CT image

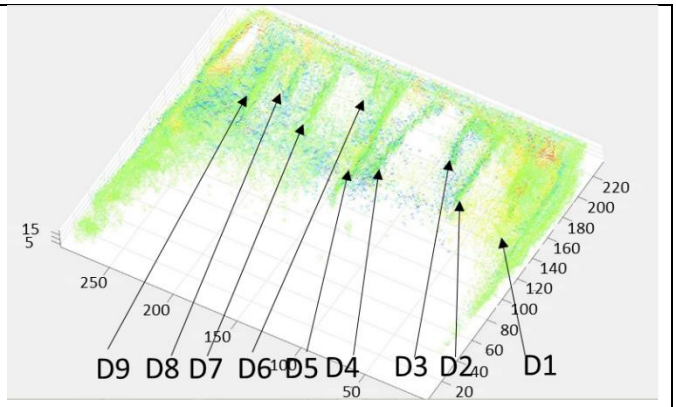

(b) Reconstructed thermal tomography image

Fig. 9 X-ray CT image and the proposed thermal tomography image (160 kV microfocus)

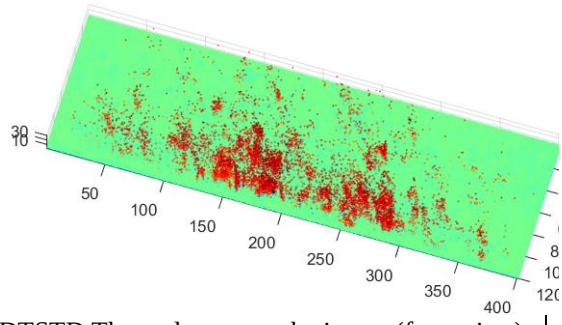

(a) DTSTD Thermal tomography image (front view)

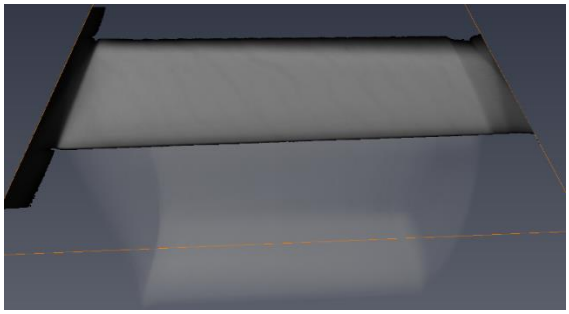

(b) X-ray tomography image

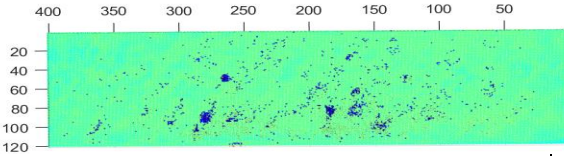

(c) DTSTD Thermal tomography image (back view)

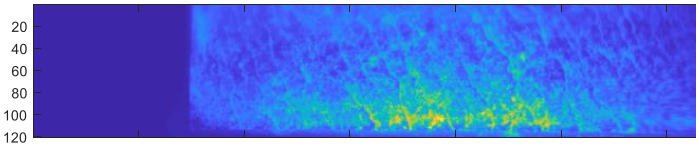

(d) Thermal image

Fig. 10 X-ray CT image and the proposed thermal tomography image (160 kV microfocus industrial CT)

Fig. 10 shows another rail track sample with tiny RCF cracks. The proposed DTSTD thermal tomography image is given in Figs 10(a) and (c). Fig. 10(d) is the thermal image and the corresponding X-ray tomography image is shown in Fig. 10(b). The excitation coil used is the Helmholtz coil located on the top and bottom side of the sample. The heating time is 200ms with current density of 230A. From the thermal image, non-uniform heating happens where the bottom side near the coil has larger mean temperature. The effect is also shown in the thermal tomography image as the bottom side has more defect points. Limited by the resolution of the thermal camera the point cloud of the RCF defect can be improved using thermal camera with higher capturing speed of transient images [30]. The defect shape, sizing and the position from the X-ray tomography will be further investigated with the DTSTD thermal tomography.

IV Conclusion and Future Work

This paper has proposed a thermal tomographic analysis of the RCF in rail track head. The square root time of temperature drop has been used to estimate the depth position. As for the response signal of crack information, the DTSTD is proposed to construct the sectional images. This work has been validated using artificial angular cracks and X-ray CT. The obtained result has shown that the DTSTD can be used as the governing pattern to reconstruct thermal tomography images, and demonstrated that thermal penetration can be modeled and applied for the 3D reconstruction of ECPT. In addition, the proposed method has better reconstruction performance than DTT method.

At present, this work reconstructs the 3D thermograph model from one single excitation angle. This poses a limitation of the reconstruction precision of the different locations of defects, sample geometry and sizes. Also, different excitation and coil angles can affect the reconstruction result. Further work will be validated through more samples of natural RCF samples with different excitation coils and angles.

V Acknowledgement

This work is supported by Natural Science Foundation of China (Grant No.61527803, and Grant No.51505308) and International Science and Technology Innovation Cooperation Project of Sichuan Province, China (Grant No. 2021YFH0036).

Reference

[1] S. L. Grassie, “Rolling contact fatigue on the British railway system:Treatment,” Wear, vol. 258, pp. 1310–1318, 2005.

[2] R. Clark, “Rail flaw detection: Overview and needs for future developments,” NDT & E Int., vol. 37, pp. 111–118, 2004.

[3] Y. Li et al., “Numerical simulation on magnetic flux leakage evaluation at high speed,” NDT & E Int., vol. 39, pp. 367–373, 2006.

[4] H. M. Thomas et al., “Advantage of a combined ultrasonic and eddy current examination for railway inspection trains,” Insight-Non-Destructive Testing Cond. Monitoring, vol. 49, pp. 341–344, 2007.

[5] G. L. Nicholson and C. L. Davis, “Modelling of the response of an ACFM sensor to rail and rail wheel RCF cracks,” NDT & E Int., vol. 46, pp. 107–114, 2012.

[6] M. Hirao and H. Ogi, EMATs for Science and Industry: Noncontacting Ultrasonic Measurements. New York: Springer Science & Business Media, 2013.

[7] D. P. Almond et al., “Thermographic techniques for the detection of cracks in metallic components,” Insight-Non-Destructive Testing Condition Monit., vol. 53, pp. 614–620, 2011.

[8] I. Mukriz et al., “3D transient magnetic field mapping for angular slots in aluminium,” Insight-Non-Destructive Testing Condition Monit., vol. 51,pp. 21–24, 2009.

[9] I. Z. Abidin et al., “Quantitative evaluation of angular defects by pulsed eddy current thermography,” NDT & E Int., vol. 43, pp. 537–546, 2010.

[10] J. Peng, G. Y. Tian, L. Wang, Y. Zhang, K. Li, and X. Gao, "Investigation into eddy current pulsed thermography for rolling contact fatigue detection and characterization," NDT & E International, vol. 74, pp. 72-80, 2015.

[11] A. Keprate and R. C. Ratnayake, “Probability of detection as a metric for quantifying NDE capability: The state of the art,” J. Pipeline Eng., vol. 14, pp. 199–209, 2015.

[12] L. Cheng, B. Gao, G. Y. Tian, W. L. Woo, and G. Berthiau, "Impact damage detection and identification using eddy current pulsed thermography through integration of PCA and ICA," IEEE Sensors Journal, vol. 14, pp. 1655-1663, 2014.

[13] J. Liu, W. Ren, G. Y. Tian, B. Gao, J. S. Meng, and Y. Wang, "Early contact fatigue evaluation of gear using eddy current pulsed thermography," in 2014 IEEE Far East Forum on Nondestructive Evaluation/Testing, pp. 208-212, 2014.

[14] Y. He, G. Tian, M. Pan, and D. Chen, "Eddy current pulsed phase thermography and feature extraction," Applied Physics Letters, vol. 103, p. 084104, 2013.

[15] L. Bai, B. Gao, G. Y. Tian, W. L. Woo, and Y. Cheng, "Spatial and time patterns extraction of eddy current pulsed thermography using blind source separation," IEEE Sensors Journal, vol. 13, pp. 2094-2101, 2013.

[16] J. Zhu, G. Tian, Q. Min, and J. Wu, Comparison Study of Different Features for Pocket Length Quantification of Angular Defects Using Eddy Current Pulsed Thermography. IEEE Transactions on Instrumentation and Measurement, 68 (5), pp. 1373-1381, 2019.

[17] Q. Yi, etc., Inverse reconstruction of fiber orientation in multi-layer CFRP using forward FEM and eddy current pulsed thermography, submitted to NDT and E International, subject to minor revision.

[18] Malcolm, Andrew A., Tong Liu, and Joseph J. Lifton. "Case studies in the use of computed tomography for non-destructive testing, inspection and measurement." Singapore International NDT Conference and Exhibition. 2013.

[19] M. Daigle, D. Fratta, and L. B. Wang. "Ultrasonic and X-ray tomographic imaging of highly contrasting inclusions in concrete specimens." Site Characterization and Modeling, pp. 1-12, 2005.

[20] Liu, X., Wang, H., Xu, M., Nie, S., & Lu, H. "A wavelet-based single-view reconstruction approach for cone beam x-ray luminescence tomography imaging.", Biomedical optics express, 5(11), pp. 3848-3858, 2014.

[21] Liu, T., Rong, J., Gao, P., Liang, Z., Zhang, W., Zhang, Y., & Lu, H. "Cone-beam x-ray luminescence computed tomography reconstruction from single-view based on total variance." In Medical Imaging: Physics of Medical Imaging ,Vol. 10573, p. 1057336, 2018.

[22] H. D. Sarkissian, et al. "A cone-beam X-ray computed tomography data collection designed for machine learning." Scientific data 6(1), pp. 1-8, 2019

[23] Gao, P., Rong, J., Pu, H., Liu, T., Zhang, W., Zhang, X., & Lu, H. "Sparse view cone beam X-ray luminescence tomography based on truncated singular value decomposition." Optics express, 26(18), pp. 23233-23250, 2018.

[24] Scopigno, Roberto, Paolo Cignoni, Marco Callieri, Fabio Ganovelli, Gaetano Impoco, Paolo Pingi, and Federico Ponchio. "Using optically scanned 3D data in the restoration of Michelangelo's David." In Optical metrology for arts and multimedia, vol. 5146, pp. 44-53. International Society for Optics and Photonics, 2003.

[25] Chen, Xiaotian, et al. "Feature based Registration for 3D Eddy Current Pulsed Thermography." IEEE Sensors Journal, 19(16) , pp. 6998 – 7004, 2019 .

[26] Chen, Xiaotian, et al. "Investigation of Skewness Feature for Evaluation of Defects Using Eddy Current Pulsed Thermography." IEEE Sensors Journal, 19(24), pp. 12118-12125, 2019

[27] Oswald-Tranta, Beata. "Thermoinductive investigations of magnetic materials for surface cracks." Quantitative InfraRed Thermography Journal 1, no. 1 (2004): 33-46.

[28] Vavilov, Vladimir P., and Marina V. Kuimova. "Dynamic thermal tomography of composites: a comparison of reference and reference-free approaches." Journal of Nondestructive Evaluation 38.1 (2019): 1-13.

[29] Vavilov, Vladimir P. "Dynamic thermal tomography: Recent improvements and applications." NDT & E International 71 (2015): 23-32.

[30] J Zhu, PJ Withers, J Wu, F Liu, Q Yi, Z Wang, GY Tian, Characterization of Rolling Contact Fatigue Cracks in Rails by Eddy Current Pulsed Thermography, IEEE Transactions on Industrial Informatics, vol. 17, no. 4, pp. 2307-2315, April 2021.